Optical Mode Control by Geometric Phase in Quasicrystal Metasurface

Igor Yulevich, Elhanan Maguid, Nir Shitrit, Dekel Veksler, Vladimir Kleiner, and Erez Hasman*
Micro and Nanooptics Laboratory, Faculty of Mechanical Engineering, and Russell Berrie Nanotechnology Institute, Technion—Israel Institute of Technology, Haifa 32000, Israel
(Received 15 February 2015; published 9 November 2015)

We report on the observation of optical spin-controlled modes from a quasicrystalline metasurface as a result of an aperiodic geometric phase induced by anisotropic subwavelength structure. When geometric phase defects are introduced in the aperiodic structured surface, the modes exhibit polarization helicity dependence resulting in the optical spin-Hall effect. The radiative thermal dispersion bands from a quasicrystal structure are studied where the observed bands arise from the optical spin-orbit interaction induced by the aperiodic space-variant orientations of anisotropic antennas. The optical spin-flip behavior of the revealed modes that arise from the geometric phase pickup is experimentally observed within the visible spectrum by measuring the spin-projected diffraction patterns. The introduced ability to manipulate the light-matter interaction of quasicrystals in a spin-dependent manner provides the route for molding light via spin-optical aperiodic artificial planar surfaces.

DOI: 10.1103/PhysRevLett.115.205501 PACS numbers: 61.44.Br, 44.40.+a, 73.20.Mf, 78.67.Pt

The discovery of quasicrystals (QCs) has changed the nature of crystallography by redefining the terminology of a crystal. QCs constitute an intermediate phase between fully periodic and fully disordered media; they lack periodicity but exhibit long-range ordering. As a result, the diffraction pattern of QCs consisting of sharp and discrete peaks reveals the rotational symmetries forbidden to ordinary crystals, including fivefold symmetry. QCs were first observed via an electron diffraction from a synthesized metallic alloy [1,2], while more recently, natural QCs have been found [3]. Quasicrystalline ordering has attracted extensive attention in various realms such as architecture, mathematics, chemistry, solid-state physics, and optics [4]. The light-matter interaction in QC structures is intriguing since it is manifested by peculiar properties such as a complete photonic band gap [5], lasing [6], localization and enhanced transport [7,8], topological phase transitions [9], optical frequency conversion [10], and superoscillations [11]. An additional twist in this field originates from the implementation of photonic QCs by metasurfaces, i.e., ultrathin two-dimensional metamaterials consisting of subwavelength meta-atoms (optical nanoantennas). Metasurfaces have triggered enormous interest as they may replace bulky optical components with ultrathin elements, paving the way for planar photonics [12–15]. Moreover, metasurfaces provide a new approach to investigate the impact of the structural symmetry on the light-matter interaction [15], which can leverage the crystallographic characteristic of complex systems. Recently, it has been shown that metallic QC metasurfaces (QCMs) consisting of isotropic nanoantennas exhibit sharp transmission resonances governed by a quasimomentum conservation rule $\mathbf{k}_{\parallel} + \mathbf{G} = \mathbf{k}_{\mathrm{SPP}}$ [16–20]. Here, $\mathbf{k}_{\mathrm{SPP}}$ is the wave vector of surface plasmon polaritons, i.e., surface-confined waves arising from the coupling of an electromagnetic field with the collective oscillations of quasifree electrons at the metal surface, $\mathbf{k}_{\parallel}$ is the wave vector of the in-plane component of the incident illumination, and $\mathbf{G}$ is any vector from the discrete reciprocal space of the QC.

Metasurfaces can also be formed by replacing the isotropic building block by its anisotropic counterpart, e.g., rod antennas. It has been shown that periodic metasurfaces consisting of anisotropic nanoantennas with space-variant orientations $\theta(x, y)$ have such a significant effect on the structure factor that requires a correction term $\mathbf{G}_c \propto \nabla\theta(x, y)$ to the momentum-matching selection rule [15,21]. This modification was manifested by the observation of new optical modes attributed to the geometric phase pickup of $2\sigma_{\pm}\theta(x, y)$ acquired due to the manipulation of the polarization state of light in the anisotropic metasurface [14,22,23]. Here $\sigma_{\pm} = \pm 1$ denotes the polarization helicity (photon spin in $\hbar$ units) corresponding to right and left circular polarizations, respectively. Note that this phase manifests itself by a geometric origin, and it differs from a dynamic phase arising from optical path differences [24]. In periodic metasurfaces with broken inversion symmetry, the optical spin degeneracy is removed, and the light-matter interaction is manifested by the optical spin-Hall effect (OSHE) [15,21,23,24], which is the optical counterpart of the spin-Hall effect in electronic transport [25]. In light of the above, it is of a great interest to investigate the influence of the local anisotropy on the light-matter interaction in QCMs, which are structures without inversion symmetry while possessing a rotational symmetry. In this Letter, we report on the observation of unique discrete optical modes of a QCM as a result of an aperiodic geometric phase induced by anisotropic antennas. These modes exhibit a remarkable OSHE in QCMs when defects in the geometric phase are introduced.

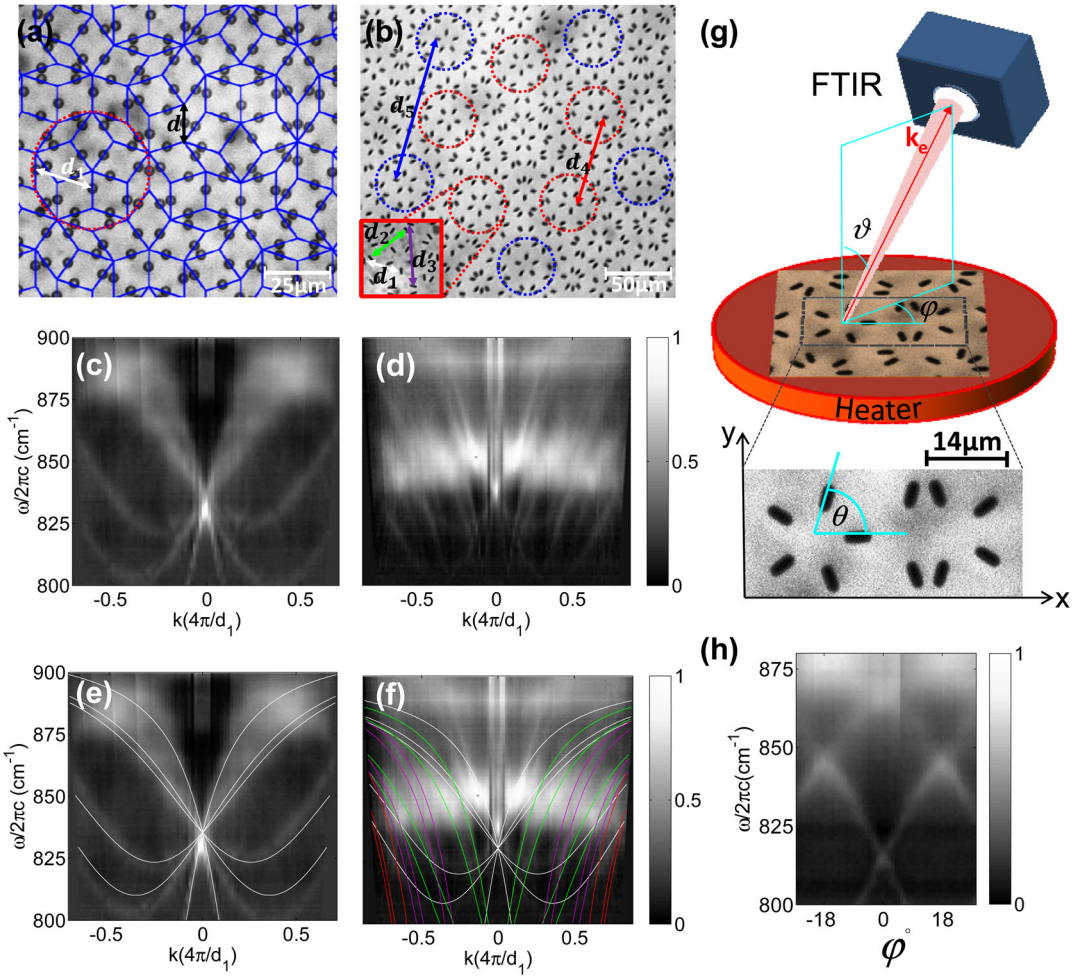

FIG. 1 (color online). Thermal emission from isotropic and anisotropic QCMs of size 8×8 mm^2. (a) Optical microscope image of the isotropic QCM, where the blue grid depicts the Penrose tiling with a side length of the rhombuses of $d = 14$ μm. Red dashed circle represents the cluster of antennas with fivefold rotational symmetry in the real space, while the white arrow is the characteristic distance d_1 between the isotropic voids with a radius of 1.75 μm, etched to a depth of 1.2 μm on a SiC substrate. (b) Optical microscope image of an anisotropic QCM consisting of 1×4 μm^2 rod voids etched to a depth of 1.2 μm on a SiC substrate. Red and blue circles depict two clusters of nanoantennas (each is rotated by 36° with respect to the others), where white, green, and purple arrows represent characteristic distances d_1, d_2, and d_3 between the anisotropic antennas (see inset); d_4 (red) and d_5 (blue) are intercluster distances. (c),(d) Dispersion $\omega(k)$ of thermal emission measured at varying polar $\vartheta \in [-50°, 50°]$ angles and a fixed azimuthal angle $\varphi = 3°$ [see Fig. 1(g)] for isotropic and anisotropic QCMs, respectively. (e),(f) Momentum-matching calculation of dispersions [based on reciprocal vectors presented in Figs. 2(c) and 2(d)] superimposed on the measurements. Red, purple, and green lines in (f) highlight the new modes in the anisotropic QCM, while the white calculated modes in (e) and (f) are the signature of the isotropic structure. (g) Schematic setup for the dispersion measurement from QCMs. The thermal emission is resolved with the FTIR, $\mathbf{k}_e$ is a wave vector of the emitted light, ϑ is the emission polar angle, φ stands for the azimuthal angle, and θ is the local orientation of the anisotropic nanoantenna. (h) Measured angle-resolved emission spectrum of the isotropic QCM at varying φ and a fixed $\vartheta = 10°$. Thermal modes possessing tenfold rotational symmetry are clearly seen.

Photonic QCMs were implemented in a Penrose structure by the use of standard photolithography on a SiC substrate supporting resonant collective lattice vibrations [surface phonon polaritons (SPhPs) [26]] in the infrared region. An isotropic QCM used as a reference was obtained by embedding an isotropic antenna at the middle of each edge of the Penrose tiling rhombuses [Fig. 1(a)]. Then, an anisotropic QCM was introduced by replacing the isotropic antennas with their anisotropic counterparts that were oriented along the edges of the tiles [Fig. 1(b)] (see, also, the Supplemental Material [27], Sec. 1). In such an arrangement, the orientation angles $\theta \in \{0°, 36°, 72°, 108°, 144°\}$ [Fig. 1(g)] correspond to the inherent anisotropy of the tiling building blocks [27]. Specifically, the QCMs were designed with the side length of the rhombuses $d = 14$ μm to match the spectral region of SiC where surface waves of SPhPs are supported. We measured the angle-resolved thermal emission spectra by a Fourier transform infrared spectrometer

(FTIR) at varying polar and fixed azimuthal angles (ϑ, φ), respectively, while heating the samples to 773 K [see Fig. 1(g)]. The observed dispersion of the anisotropic QCM [Fig. 1(d)] reveals new collective modes as compared to the isotropic QC [Fig. 1(c)], which may give rise to geometric phase bands due to the space-variant orientation of the antennas.

To analyze the experimental results, we calculated the structure factor, i.e., the momentum space of the isotropic QCM by the Fourier transform $\hat{F}$ of the nanoantenna positions $\mathbf{r}_n$ in the real space $f_0(\mathbf{k}) = \hat{F}[\sum_n \delta(\mathbf{r} - \mathbf{r}_n)]$ [Fig. 2(c)]. The structure factor reveals a discrete wave vector set $\mathbf{G}_1$ with tenfold rotational symmetry in the reciprocal space associated with the characteristic distance d_1 in the QC structure via the relation $|\mathbf{G}_1| = 4\pi/d_1$ [16], where $d_1 = d\tau$ and $\tau = (1+\sqrt{5})/2$ is the golden ratio [Fig. 1(a)]. The measured dispersion relation of the isotropic QCM [Fig. 1(c)] exhibits good agreement with the calculation based on the momentum-matching equation $\mathbf{k}_{e\|} + \mathbf{G} = \mathbf{k}_{\mathrm{SPhP}}$ [Fig. 1(e)]. Here, $\mathbf{k}_{e\|}$ is the wave vector component of the emitted light in the surface plane, and $\mathbf{k}_{\mathrm{SPhP}}$ is the SPhP momentum. For an analogous calculation in the case of the anisotropic QCM, the orientation degree of freedom $\theta(\mathbf{r}_n)$ must be taken into account. It was previously shown that the localized mode resonance of an anisotropic void antenna is observed with a linear polarization excitation parallel to its minor axis [23,30,31] (see, also, the Supplemental Material [27], Sec. 2). When such a dipole antenna is interacting with circularly polarized light, a local phase pickup delay of $2\sigma_{\pm}\theta$ is induced. Thus, the momentum space of the anisotropic QCM is given by $f_{\pm}(\mathbf{k}) = \hat{F}[\sum_n \delta(\mathbf{r} - \mathbf{r}_n) e^{i2\sigma_{\pm}\theta(\mathbf{r}_n)}]$ with an additional geometric phase factor corresponding to the orientational degree of freedom [see Fig. 2(d)]. Specifically, in the introduced anisotropic QCM, the orientation angle of the rod antennas, which is mod π defined, is discrete due to the Penrose tiling process, i.e., $\theta \in \{0°, 36°, 72°, 108°, 144°\}$; as a result, the geometric phase is five levels quantized. Figure 2(d) shows the wave numbers $|\mathbf{G}_m| = 4\pi/d_m$ $(m = 1, ..., 5)$ with tenfold rotational symmetry that are located on five circles in the momentum space, where the four inner circles $(m = 2, ..., 5)$ reveal the new wave numbers, whereas the outer circle of modes $(m = 1)$ coincides with the isotropic structure states [compare to Fig. 2(c)]. The characteristic distances of the anisotropic QCM depicted in Fig. 1(b) are defined via $d_{1,...,5} = d\{\tau, \gamma, \tau^2, \tau^2\gamma, \tau^3\gamma\}$, where $\gamma = \sqrt{\tau + 2}$. By considering the corresponding momentum space [Fig. 2(d)], we calculated the dispersion of the anisotropic QCM according to the quasimomentum conservation. The result [Fig. 1(f)] confirms the measured dispersion [Fig. 1(d)] and reveals the new modes in comparison to the isotropic QCM. These discrete modes arise from the geometric phase term induced by the aperiodic space-variant orientations of the antennas. Such a phenomenon is supported by observation of spectral plasmonic resonances originated from the geometric phase pickup within the visible transmission spectrum of a metal structured surface (Supplemental Material [27], Sec. 3). Moreover, the polarization-resolved measurement of the thermal emission revealed that the QC modes are polarization-helicity degenerated. This result is in agreement with the calculation of the Fourier amplitudes $|f_{\pm}(\mathbf{k})|$ for the $\sigma_{\pm}$ helicities of the emerging field, and it originates from the rotational symmetry of the structures [32].

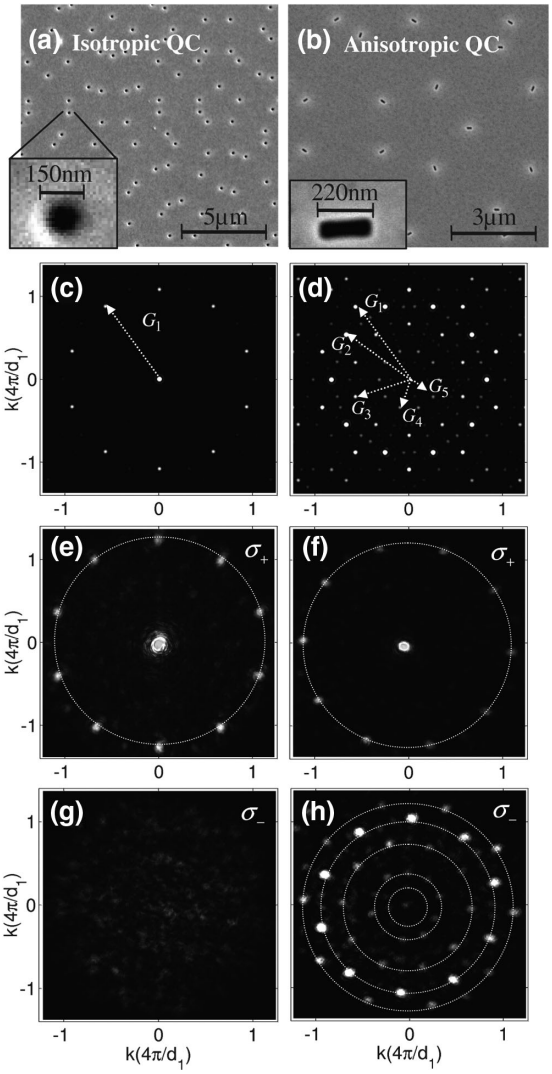

FIG. 2. (a),(b) Scanning electron microscope images of isotropic and anisotropic QCMs of the size 60×60 μm^2. The side of the tiling rhombi is $d = 2.5$ μm, where holes of radius 60 nm (a) and 80×220 nm^2 rod apertures (b) were perforated in a 200 nm thick Au film. (c),(d) Calculated diffraction intensities of the isotropic $|f_0(\mathbf{k})|^2$ (c) and anisotropic $|f_{\pm}(\mathbf{k})|^2$ (d) QCMs. (e),(g) Measured diffraction patterns of the two helicity components of isotropic QCM: the incident helicity state σ_+ (e) and the spin-flip state σ_- (g). (f),(h) Measured diffraction patterns of anisotropic QCM of the incident helicity state σ_+ (f) and the spin-flip state σ_- (h) components.

We further investigated the optical modes induced by the geometric phase in the anisotropic QCM and specifically the polarization of light interacting with the QCM, within the visible spectrum. By reducing the length scale, we fabricated nanoscale isotropic and anisotropic QCMs using a Ga^+ focused ion beam [Figs. 2(a) and 2(b)]. The samples were sandwiched between circular polarizers and normally illuminated with a continuous wave Ti:sapphire tunable laser at a wavelength of 750 nm, whereas the initial polarizer determines the incident polarization helicity of $\sigma_\pm$. The spin-projected intensity distribution was measured in the far field, which corresponds to the momentum space. The observed diffraction pattern from the isotropic QCM maintains the incident polarization [compare Figs. 2(e) and 2(g)] and confirms the single circle of modes with tenfold symmetry and a wave number of $|\mathbf{G}_1|$. Polarization analysis of the anisotropic QCM shows that the diffraction pattern contains both the incident helicity state σ_+ [Fig. 2(f)] and the opposite (spin-flip) state σ_- [Fig. 2(h)]. The σ_+ component is a signature of the structural contribution to the QCM modes with the wave number $|\mathbf{G}_1|$, while the spin-flip component reveals five circles of modes associated with the wave numbers $|\mathbf{G}_{1,\ldots,5}|$ corresponding to the geometric phase contribution (Supplemental Material [27], Sec. 4). Such a polarization analysis provides the route to control the diffraction of the QCMs in a spin-dependent manner. Note that the same behavior of the diffraction pattern is obtained for the incident polarization state of σ_- [27].

An electronic spin-Hall effect induced by impurities [33] inspires one to investigate the OSHE in an anisotropic QCM due to defects in the aperiodic geometric phase and to obtain spin-orbit interaction of light; i.e., spin and orbital properties become strongly coupled with each other [24]. In order to observe the OSHE in QCMs, we randomly selected nanoantennas wherein the orientations were randomly chosen from a uniform angle distribution. For a specific outcome of the randomization process, where the defects constitute half of the antennas composing the QCM, we obtained a distorted QC structure with $d = 2.5\ \mu$m [Fig. 3(a)]. The QCM was illuminated with right and left circularly polarized light at the wavelength of $\lambda = 750$ nm and a spin-dependent diffraction pattern associated with the OSHE is observed [Figs. 3(d)–3(f)]. The OSHE in the QCM was verified by calculating the spin-dependent Fourier amplitudes [Figs. 3(b), 3(c), and 3(f)]. Moreover, the efficiency of the OSHE, i.e., $\eta_{\mathrm{OSHE}} = (I_{\sigma_+} - I_{\sigma_-})/(I_{\sigma_+} + I_{\sigma_-})$, where $I_{\sigma_\pm}$ are the intensities of a specific mode for $\sigma_\pm$ incident helicities, respectively, is strongly affected by the concentration of the defects; it increases significantly when the concentration reaches a critical value corresponding to the mean distance between defects $a^* \leq d$ [Fig. 3(g)]. Note that the OSHE efficiency for the different modes ($\mathbf{G}_m$) of the anisotropic QCM depends on the randomization process (see Supplemental Material [27], Sec. 5). Inserting defects in the geometric phase ushers in violating the rotational symmetry of the QCM that enables the spin-degeneracy removal of the optical modes.

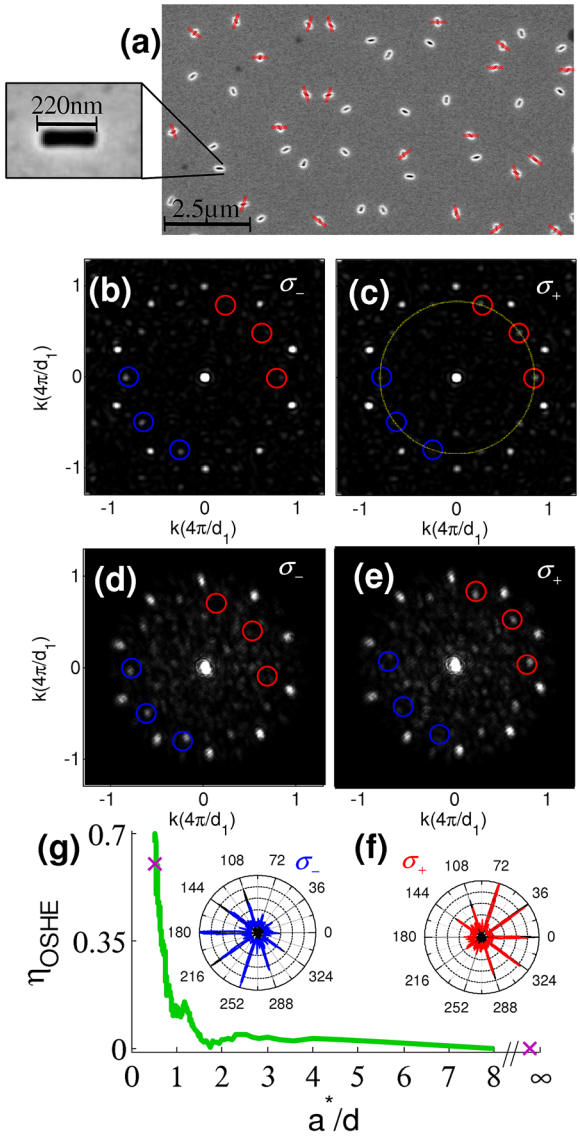

FIG. 3 (color online). (a) SEM image of the anisotropic QCM with the orientational defects. Size parameters are the same as in Fig. 2(b). Red lines denote the original antenna configuration. (b)–(e) Calculated (b),(c) and measured (d),(e) diffraction patterns of the QCM with the geometric phase defects. The patterns reveal the spin-dependent modes located on the $|\mathbf{G}_2|$ circle for σ_- (b),(d) and σ_+ (c),(e) illuminations, respectively. Blue and red guiding rings highlight the location of the spin-dependent modes in the reciprocal space for each helicity $\sigma_\pm$. (f) Azimuthal cross sections of measured (red and blue) and calculated (black) intensities for $\sigma_\pm$ illuminations. The intensities were measured along the yellow circle in (c). In this polar representation, the azimuthal angle is given in degrees and the intensity is on a linear scale. (g) Dependence of the OSHE efficiency η_{OSHE} on the normalized average distance between defects a^*/d. The green curve corresponds to the calculated efficiency for the specific randomization process and the experimental points are denoted by purple crosses.

In summary, we observed strongly affected optical modes of QCM as a result of the aperiodic geometric phase induced by anisotropic nanoantennas. The presented momentum space analysis reveals the effect of the nanoantenna orientations on the light-matter interaction in QCMs. The introduced ability to remove the spin degeneracy in QCMs by inserting defects in the aperiodic geometric phase paves the way for controlling light transport via the spin-optical aperiodic metasurfaces. The reported phenomena can be extended to dielectric materials, where the polarization anisotropy of the individual building block can be obtained through Mie resonances.

This research was supported by the Israel Science Foundation, the Israel Nanotechnology Focal Technology Area on Nanophotonics for Detection, and KLA-Tencor.

*mehasman@technion.ac.il

[1] D. Shechtman, I. Blech, D. Gratias, and J. W. Cahn, Phys. Rev. Lett. **53**, 1951 (1984).
[2] D. Levine and P. J. Steinhardt, Phys. Rev. Lett. **53**, 2477 (1984).
[3] L. Bindi, P. J. Steinhardt, N. Yao, and P. J. Lu, Science **324**, 1306 (2009).
[4] Z. V. Vardeny, A. Nahata, and A. Agrawal, Nat. Photonics **7**, 177 (2013).
[5] M. E. Zoorob, M. D. B. Charlton, G. J. Parker, J. J. Baumberg, and M. C. Netti, Nature (London) **404**, 740 (2000).
[6] M. Notomi, H. Suzuki, T. Tamamura, and K. Edagawa, Phys. Rev. Lett. **92**, 123906 (2004).
[7] M. Segev, Y. Silberberg, and D. N. Christodoulides, Nat. Photonics **7**, 197 (2013).
[8] L. Levi, M. Rechtsman, B. Freedman, T. Shwartz, O. Manela, and M. Segev, Science **332**, 1541 (2011).
[9] M. Verbin, O. Zilberberg, Y. E. Kraus, Y. Lahini, and Y. Silberberg, Phys. Rev. Lett. **110**, 076403 (2013).
[10] R. Lifshitz, A. Arie, and A. Bahabad, Phys. Rev. Lett. **95**, 133901 (2005).
[11] F. M. Huang, N. Zheludev, Y. Chen, and F. J. Garcia de Abajo, Appl. Phys. Lett. **90**, 091119 (2007); F. M. Huang, Y. Chen, F. J. Garcia de Abajo, and N. I. Zheludev, J. Opt. A **9**, S285 (2007).
[12] A. V. Kildishev, A. Boltasseva, and V. M. Shalaev, Science **339**, 1232009 (2013).
[13] N. Yu and F. Capasso, Nat. Mater. **13**, 139 (2014).
[14] D. Lin, P. Fan, E. Hasman, and M. L. Brongersma, Science **345**, 298 (2014).
[15] N. Shitrit, I. Yulevich, E. Maguid, D. Ozeri, D. Veksler, V. Kleiner, and E. Hasman, Science **340**, 724 (2013).
[16] T. Matsui, A. Agrawal, A. Nahata, and Z. V. Vardeny, Nature (London) **446**, 517 (2007).
[17] N. Papasimakis, V. A. Fedotov, A. S. Schwanecke, N. I. Zheludev, and F. J. Garcia de Abajo, Appl. Phys. Lett. **91**, 081503 (2007).
[18] C. Bauer, G. Kobiela, and H. Giessen, Sci. Rep. **2**, 681 (2012).
[19] D. Pacifici, H. J. Lezec, L. A. Sweatlock, R. J. Walters, and H. A. Atwater, Opt. Express **16**, 9222 (2008).
[20] F. Przybilla, C. Genet, and T. W. Ebbesen, Appl. Phys. Lett. **89**, 121115 (2006).
[21] N. Dahan, Y. Gorodetski, K. Frischwasser, V. Kleiner, and E. Hasman, Phys. Rev. Lett. **105**, 136402 (2010).
[22] Z. Bomzon, G. Biener, V. Kleiner, and E. Hasman, Opt. Lett. **27**, 1141 (2002).
[23] N. Shitrit, I. Bretner, Y. Gorodetski, V. Kleiner, and E. Hasman, Nano Lett. **11**, 2038 (2011).
[24] K. Y. Bliokh, F. J. Rodríguez-Fortuño, F. Nori, and A. V. Zayats, arXiv:1505.02864v2.
[25] M. I. Dyakonov and V. I. Perel, Phys. Lett. A **35**, 459 (1971).
[26] J. J. Greffet, R. Carminati, K. Joulain, J. P. Mulet, S. Mainguy, and Y. Chen, Nature (London) **416**, 61 (2002).
[27] See the Supplemental Material at http://link.aps.org/supplemental/10.1103/PhysRevLett.115.205501 for the tiling rule of antenna configurations, local modes of the QCMs, transmission spectra of plasmonic-based QCMs, far-field radiation from the anisotropic QCM, and optical spin-Hall effect for different outcomes of the randomization process, which includes Refs. [28,29].
[28] K. D. Ko and C. K. Toussaint, J. Quant. Spectrosc. Radiat. Transfer **110**, 1037 (2009).
[29] J. D. Jackson, *Classical Electrodynamics*, 3rd ed. (John Wiley & Sons, Inc., New York, 1999).
[30] R. Gordon, A. G. Brolo, A. McKinnon, A. Rajora, B. Leathem, and K. L. Kavanagh, Phys. Rev. Lett. **92**, 037401 (2004).
[31] K. Frischwasser, I. Yulevich, V. Kleiner, and E. Hasman, Opt. Express **19**, 23475 (2011).
[32] S. S. Kruk, C. Helgert, M. Decker, I. Staude, C. Menzel, C. Etrich, C. Rockstuhl, C. Jagadish, T. Pertsch, D. N. Neshev, and Y. S. Kivshar, Phys. Rev. B **88**, 201404 (2013).
[33] Y. Niimi, M. Morota, D. H. Wei, C. Deranlot, M. Basletic, A. Hamzic, A. Fert, and Y. Otani, Phys. Rev. Lett. **106**, 126601 (2011).